

# Formation of Galactic Center Magnetic Loops

Mami MACHIDA

*Division of Theoretical Astronomy, National Astronomical Observatory of Japan,  
Osawa, Mitaka, Tokyo 181-8588, Japan*

*mami@th.nao.ac.jp*

Ryoji MATSUMOTO

*Faculty of Science, Chiba University, Yayoi-cho, Inage-ku, Chiba, 263-8522, Japan*

Satoshi NOZAWA

*Department of Science, Ibaraki University, 2-1-1 Bunkyo, Mito, Ibaraki 310-8512, Japan*

Kunio TAKAHASHI

*CfCA, National Astronomical Observatory of Japan, Osawa, Mitaka, Tokyo 181-8588, Japan*

Yasuo FUKUI, Natsuko KUDO, Kazufumi TORII, Hiroaki YAMAMOTO, Motosuji FUJISHITA

*Department of Astrophysics, Nagoya University, Chikusa-ku, Nagoya 464-8602, Japan*

and

Kohji TOMISAKA

*Division of Theoretical Astronomy, National Astronomical Observatory of Japan,  
Osawa, Mitaka, Tokyo 181-8588, Japan*

(Received 2000 December 31; accepted 2001 January 1)

## Abstract

A survey for the molecular clouds in the Galaxy with NANTEN mm telescope has discovered molecular loops in the Galactic center region. The loops show monotonic gradients of the line of sight velocity along the loops and the large velocity dispersions towards their foot points. It is suggested that these loops are explained in terms of the buoyant rise of magnetic loops due to the Parker instability. We have carried out global three-dimensional magneto-hydrodynamic simulations of the gas disk in the Galactic center. The gravitational potential is approximated by the axisymmetric potential proposed by Miyamoto & Nagai (1975). At the initial state, we assume a warm ( $\sim 10^4\text{K}$ ) gas torus threaded by azimuthal magnetic fields. Self-gravity and radiative cooling of the gas are ignored. We found that buoyantly rising magnetic loops are formed above the differentially rotating, magnetically turbulent disk. By analyzing the results of global MHD simulations, we have identified individual loops, about 180 in the upper half of the disk, and studied their statistical properties such as their length, width, height, and velocity distributions along the loops. Typical length and height of a loop are 1kpc and 200pc, respectively. The line of sight velocity changes linearly along a loop and shows large dispersions around the foot-points.

Numerical results indicate that loops emerge preferentially from the region where magnetic pressure is large. We argue that these properties are consistent with those of the molecular loops discovered by NANTEN.

**Key words:** Galaxy: Magnetic field, MHD, Magnetic loops, ISM

## 1. Introduction

Spiral galaxies generally possess large-scale magnetic fields (e.g., Sofue et al. 1986; Beck et al. 1996). These magnetic fields are usually considered to be amplified and maintained by large-scale dynamo action driven by collective inductive effects of turbulence and differential rotation (Parker 1971). In our Galaxy, the strength of the magnetic field is about a few  $\mu$  G. Inside 200pc from the Galactic center, however, radio observations indicate that magnetic fields are as strong as a few mG (e.g., Morris & Serabyn 1996). Recent observations of other spiral galaxies indicate that the typical averaged equipartition strength of the total magnetic fields is about  $10\mu$ G (Beck 2008).

Based on a survey for the molecular gas in the Galaxy by NANTEN (e.g., Mizuno & Fukui 2004). Fukui et al. (2006) found loop-like structures of dense molecular gas showing large line-of-sight velocity gradients ( $\sim 30$ km/s) along the loops and large velocity dispersions at their foot-points. The total mass of the molecular gas estimated from the observation is about  $1.7 \times 10^5 M_{\odot}$  when LTE at 50K was assumed at a distance of 8.5 kpc. The kinetic energy of the loops estimated from their line-of-sight velocity gradient exceeds  $10^{51}$  ergs. This energy exceeds the energy injected by a supernova and requires other energetic mechanisms driving the molecular gas.

The velocity gradient along the loops and large velocity dispersions at their foot-points are typical features of solar magnetic loops emerging from below the photosphere. The emergence of solar magnetic loops from the photosphere to the corona is driven by the buoyancy created by sliding the gas along the loop. Even when the unperturbed atmosphere is convectively stable, the magnetic loop can rise when the buoyancy at the loop top exceeds the restoring magnetic tension. This instability is called the Parker instability. Parker instability was originally proposed as a mechanism of the formation of the interstellar clouds (Parker 1966). Matsumoto et al. (1988) carried out two-dimensional magneto-hydrodynamic (MHD) simulations of the Parker instability in astrophysical disks and showed that in the nonlinear stage of the Parker instability, shock waves are formed near the foot-points of the magnetic loops because gas slides down supersonically (e.g., Shibata et al. 1989). Such shocks can be an origin of large velocity dispersions observed near the foot-points of Galactic center molecular loops (Fukui et al. 2006).

Two-dimensional MHD simulations of the Parker instability in the Cartesian coordinate system of the gas disk can reproduce loop-like structures and velocity gradients similar to the

observed loops (Fukui et al. 2006). In their simulations, however, the Galactic rotation was not taken into account. In rotating stratified magnetized layer such as galactic gas disk, Coriolis force twists the magnetic loops. Since the twisting of magnetic fields enhances magnetic tension, the growth rate of the Parker instability is suppressed. Chou et al. (1997) carried out local three-dimensional MHD simulations of the Parker instability by using a frame corotating with the disk to consider the effect of the Coriolis force. They confirmed that the Parker instability grows in rotating disks, although growth rate becomes smaller than that without rotation.

In the gas disk rotating differentially, another instability, magneto-rotational instability (MRI) grows (Balbus & Hawley 1991). Three-dimensional local 3D MHD simulations adopting the shearing sheet approximation confirmed that MRI drives magnetic turbulence inside the disk (e.g., Hawley et al. 1995; Matsumoto & Tajima 1995; Brandenburg et al. 1995; Stone et al. 1996; Sano & Miyama 1999). When we take into account the vertical gravity, buoyantly rising magnetic loops can be formed by the Parker instability. In the Galactic center region, since the loop size must be comparable to the distance from the Galactic center, non-local effects such as curvature becomes important. Global MHD simulations of the buoyant rise of magnetic loops from differentially rotating gas disks were first carried out by Machida, Hayashi, & Matsumoto (2000). They showed that magnetic loops emerge from the turbulent disk. They assumed the gravitational force created by the central point mass. In Galactic gas disks, however, gravity is determined by stars and the dark matter.

Nishikori et al. (2006) presented the results of global three-dimensional MHD simulations of Galactic gaseous disks to study how the Galactic magnetic fields are amplified and maintained. They assumed a steady axisymmetric gravitational potential given by Miyamoto & Nagai (1975). Their simulations showed that magnetic fields are amplified up to  $\mu$  G and are maintained for 10 billion years. They also found that mean azimuthal magnetic fields reverse their direction in every 1Gyr. This field reversal is driven by the buoyant escape of magnetic flux from the disk to the Galactic halo. Their simulation region ( $0.8\text{kpc} < \varpi < 30\text{kpc}$ ), however, did not include the galactic center. Here,  $\varpi$  is the distance from the Galactic center.

Baek et al. (2008) proposed that collision of the high velocity cloud with the Galactic disk explains the formation of the molecular loop structure seen at the Galactic center, when the high velocity cloud has an oblique collision with the disk plane. They showed that the size was similar to that of the molecular loop, but the velocity gradient was smaller than that of the observation.

In this paper, we report the results of global 3D MHD simulations of Galactic central gas disks inside 1kpc from the Galactic center. In section 2, we present basic equations and describe the numerical model. Numerical results will be presented in section 3. Section 4 is devoted for discussion. Summary will be given in section 5.

**Table 1.** Parameters adopted for the gravitational potential

	$a_i$ (kpc)	$b_i$ (kpc)	$M_i(10^{10}M_\odot)$
Bulge 1	0.0	0.495	2.05
Disk 2	7.258	0.520	25.47

## 2. Numerical Methods

### 2.1. Basic equations

We solved the following MHD equations in the cylindrical coordinate system  $(\varpi, \varphi, z)$ :

$$\frac{\partial \rho}{\partial t} + \nabla \cdot (\rho \mathbf{v}) = 0, \quad (1)$$

$$\rho \left[ \frac{\partial \mathbf{v}}{\partial t} + \mathbf{v} \cdot \nabla \mathbf{v} \right] = -\nabla P - \rho \nabla \phi + \frac{\mathbf{j} \times \mathbf{B}}{c}, \quad (2)$$

$$\frac{\partial \mathbf{B}}{\partial t} = \nabla \times (\mathbf{v} \times \mathbf{B}), \quad (3)$$

$$\rho T \frac{dS}{dt} = 0, \quad (4)$$

where  $\rho$ ,  $P$ ,  $\phi$ ,  $\mathbf{v}$ ,  $\mathbf{B}$ ,  $\mathbf{j} = c\nabla \times \mathbf{B}/4\pi$ ,  $T$ , and  $S$  are the density, pressure, gravitational potential, velocity, magnetic field, current density, temperature and specific entropy, respectively. The specific entropy is expressed as  $S = C_V \ln(P/\rho^\gamma)$ , where  $C_V$  is the specific heat capacity and  $\gamma$  is the specific heat ratio.

We adopt the Galactic gravitational potential proposed by Miyamoto & Nagai (1975),

$$\phi(\varpi, z) = -\sum_{i=1,2} \frac{GM_i}{[\varpi^2 + \{a_i + (z^2 + b_i^2)^{1/2}\}^2]^{1/2}}. \quad (5)$$

Here,  $G$  is the gravitational constant. The first term ( $i = 1$ ) on the right hand side of equation (5) corresponds to the potential by bulge stars and the second term ( $i = 2$ ) corresponds to the disk component. The parameters adopted in this paper are shown in table 1.

### 2.2. Numerical Methods and Boundary Conditions

We solved the MHD equations by using a modified Lax–Wendroff scheme (Rubin & Burstein 1967) with artificial viscosity (Richtmyer & Morton 1967).

For normalization, we use the units listed in table 2. The units of length  $r_0$  and velocity  $v_0$  are 1 kpc and  $v_0 = \sqrt{GM_0/r_0}$ , respectively. Here,  $M_0 = 10^{10}M_\odot$ . Thus the unit time is equal to  $t_0 = r_0/v_0 = 4.7 \times 10^6$  year. The unit temperature is given by  $T_0 = m_p v_0^2 k_B^{-1} = 5.2 \times 10^6$  K, where  $m_p$  is the proton mass and  $k_B$  is the Boltzmann constant.

The number of grid points is  $(N_\varpi, N_\varphi, N_z) = (200, 64, 384)$ . The grid size is  $\Delta\varpi = \Delta z = 0.01$  for  $0 < \varpi < 1.2$  and  $|z| < 1.0$ , and otherwise increases with  $\varpi$  and  $z$ . The grid size in the azimuthal direction is  $\Delta\varphi = 2\pi/63$ . The outer boundaries at  $\varpi = 11.58$  and at  $|z| = 16$

**Table 2.** Units adopted in this paper.

Physical Quantity	Symbol	Numerical Unit
Length	$r_0$	1kpc
Velocity	$v_0$	207 km sec <sup>-1</sup>
Time	$t_0$	$4.7 \times 10^6$ year
Temperature	$T_0$	$5.2 \times 10^6$ K

are free boundaries where waves can be transmitted. We included the full circle ( $0 \leq \varphi \leq 2\pi$ ) in the simulation region, and applied periodic boundary conditions in the azimuthal direction. An absorbing boundary condition is imposed at  $r = (\varpi^2 + z^2)^{1/2} = r_{\text{in}} = 0.2$  by introducing a damping parameter,

$$a_d = 0.1 \left( 1.0 - \tanh \frac{r - r_{\text{in}} + 5\Delta\varpi}{2\Delta\varpi} \right). \quad (6)$$

The physical quantities  $q = (\rho, \mathbf{v}, \mathbf{B}, P)$  inside  $r = r_{\text{in}}$  are re-evaluated by

$$q^{\text{new}} = q - a_d(q - q_0), \quad (7)$$

which means that the deviation from initial values  $q_0$  is artificially reduced with a rate  $a_d$ . Thus waves propagating inside  $r = r_{\text{in}}$  are absorbed in the transition region ( $r_{\text{in}} - 5\Delta\varpi < r < r_{\text{in}}$ ).

A random perturbation is added in the azimuthal velocity at the initial state. The maximum amplitude of the perturbation is 1% of the initial azimuthal velocity at the radius.

### 2.3. Initial Model

At the initial state, we assume a gas torus around  $\varpi \sim 1\text{kpc}$ . The torus is threaded by a weak toroidal magnetic field. The initial torus is assumed to have a specific angular momentum,  $L \propto \varpi^a$ .

According to Okada et al. (1989), by using the polytropic relation  $P = K\rho^\gamma$  at the initial state and by assuming  $\beta = 8\pi P/B_\varpi^2 = \beta_b(\varpi/\varpi_b)^{1/2}$ , where  $\beta_b$  is the initial plasma  $\beta$  at the initial pressure maximum of the torus  $(\varpi, z) = (\varpi_b, 0)$ , and  $B_\varphi$  is the azimuthal magnetic field, we integrated the equation of motion into a potential form,

$$\Psi(\varpi, z) = \phi + \frac{L^2}{2\varpi^2} + \frac{1}{\gamma - 1}v_s^2 + \frac{\gamma}{2(\gamma - 1)}v_A^2 = \Psi_b = \text{constant}, \quad (8)$$

where  $v_s = (\gamma P/\rho)^{1/2}$  is the sound speed,  $v_A = [B_\varphi^2/(4\pi\rho)]^{1/2}$  is the Alfvén speed, and  $\Psi_b = \Psi(\varpi_b, 0)$ . At  $\varpi = \varpi_b$ , the rotation speed of the torus  $L/\varpi_b$  equals to the Keplerian velocity. By using equation (8), we obtain the density distribution as

$$\rho = \rho_b \left\{ \frac{\max[\Psi_b - \phi - L^2/(2\varpi^2), 0]}{K[\gamma/(\gamma - 1)][1 + \beta_b^{-1}\varpi^{2(\gamma-1)}/\varpi_b^{2(\gamma-1)}]} \right\}^{1/(\gamma-1)}, \quad (9)$$

where  $\rho_b$  is the density at  $(\varpi, z) = (\varpi_b, 0)$ . Outside the torus, we assumed a hot, isothermal

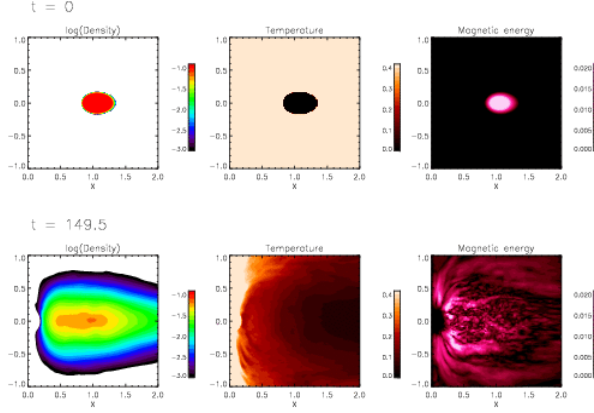


**Fig. 1.** Distribution of azimuthally averaged quantities for the initial state (top) and quasi-steady state at  $t = 149.5 = 0.7\text{Gyr}$ . Left panels show the logarithmistic density distribution. Middle panels show the azimuthally averaged temperature. Right panels show the magnetic energy.

( $T = T_{\text{halo}}$ ) spherical halo. The density distribution of the halo is given by  $\rho_{\text{h}} = \rho_{\text{halo}} \exp[-(\phi - \phi_{\text{b}})/(k_{\text{B}}T_{\text{halo}})]$ , where  $\phi_{\text{b}}$  is the gravitational potential at  $(\varpi, z) = (\varpi_{\text{b}}, 0)$ .

In this paper, we assume that the initial gas ring (torus) consists of the warm component of the interstellar gas. If we assume the cold component ( $T \sim 100\text{K}$ ), the length of the magnetic loops will be much shorter than the length of observed loops. This situation is similar to the solar emerging magnetic loops. Their length is about 3000km when they emerge from the photosphere but the loops elongate as they rise. The elongated loop length eventually exceeds  $10^4$  km in well-developed active regions. It means that their length is determined not by the photospheric temperature but rather by the coronal one. We do not include the effects of star formation, feedbacks to the gas dynamics by supernova explosions, nor winds from massive stars. The effects of the gas heating by supernova explosions are approximately taken into account by assuming warm interstellar gas whose scale height is about 150 pc at 1kpc from the galactic center. We ignore the self-gravity of the gas and the radiative cooling term. The sound speed assumed in this paper is  $v_{\text{b}} = 0.14$  at  $\varpi = \varpi_{\text{b}}$  where the gravity equals to the centrifugal force. The initial temperature at  $\varpi = \varpi_{\text{b}}$  is  $T_{\text{b}} = 0.01T_0 (= 5.2 \times 10^4 \text{ K})$ . Model parameters adopted in this paper are  $\varpi_{\text{b}} = r_0$ ,  $\beta_{\text{b}} = 10$ ,  $\gamma = 5/3$ ,  $L = (\varpi_{\text{b}}/2)^{1/2}\varpi_{\text{b}}/(\varpi_{\text{b}} - 1)\varpi^a$ ,  $a = 0.46$ , and  $\rho_{\text{halo}} = 10^{-5}\rho_{\text{b}}$ .

### 3. Numerical Results

#### 3.1. Time Evolution of the Gaseous Disks

The simulations show a general trend that the MHD instabilities take place over the entire disk and the gas is strongly driven by these instabilities. The gas temperature increases because of the dissipation of the magnetic energy in the disk.

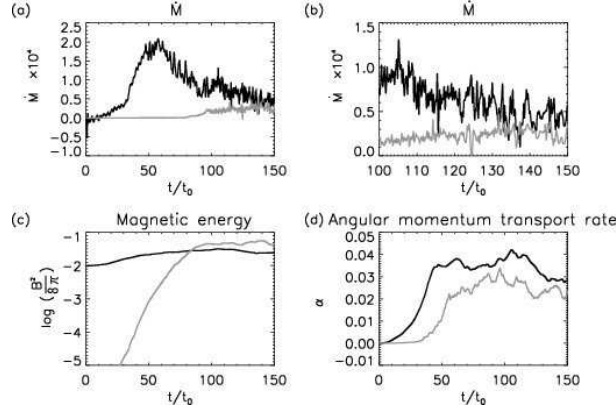


**Fig. 2.** (a) Time evolution of the mass accretion rate measured at  $\varpi = 0.8$  (black) and at  $\varpi = 0.3$  (gray). Mass accretion rate is integrated in the azimuthal direction and in  $|z| < 1$ . (b) The same as (a) but for  $100 < t/t_0 < 150$ . (c) Time evolution of the magnetic energy averaged in the vertical direction ( $|z| < 0.5$ ), in the radial direction  $0.8 < \varpi < 1.2$ , and in the azimuthal direction (black curve). Gray curve shows the magnetic energy averaged in  $0.3 < \varpi < 0.6$ ,  $|z| < 0.1$  and in the azimuthal direction. (d) Time evolution of the averaged angular momentum transport rate  $\alpha \equiv -\langle B_\varpi B_\varphi / 4\pi \rangle / \langle P \rangle$ . Black curve shows that averaged in  $0.8 < \varpi < 1.2$ , and gray curve shows that averaged in  $0.3 < \varpi < 0.6$ .

Top and bottom panels of figure 1 show the initial condition and the snapshot at  $t = 149.5$ . Left panels show the density distributions averaged in the azimuthal direction. Middle panels show the temperature distribution and right panels show the magnetic energy distribution. Owing to the angular momentum redistribution, the initial torus is deformed into a thick disk. The disk temperature increases as the disk is heated by dissipation of the magnetic energy. When matter accretes in differentially rotating disks by transporting angular momentum outward, the released gravitational energy heats the disk gas. In magnetically turbulent disks, in which the angular momentum is mainly transported by Maxwell stress, the disk is heated by the magnetic energy dissipation (e.g., Hirose, Krolik, & Stone 2006; Machida, Nakamura, & Matsumoto 2006). The gas heating which takes place in our simulations also comes from this dissipation of the magnetic energy. Bottom right panel of figure 1 shows that magnetic fields emerge from the disk and occupy the disk halo.

Figure 2a and 2b show the time evolution of the mass accretion rate. Black and gray curves show  $\dot{M}$  measured at  $\varpi = 0.8$  and  $\varpi = 0.3$ , respectively. Mass accretion takes place quasi-steadily after  $t = 100t_0$ . The mass accretion rate shows rapid time variations. Figure 2c shows the time evolution of the azimuthally averaged magnetic energy. The black curve and the gray curve depicts the magnetic energy averaged over  $|z| < 5$  in the outer region ( $0.8 < \varpi < 1.2$ ) and in the inner region ( $0.3 < \varpi < 0.6$ ), respectively. At the initial state, the plasma  $\beta$  in the outer region is  $\beta \sim 10$ . After a few dozens of rotations, the plasma  $\beta$  in the outer region stays around  $\beta \sim 10$ . The right panels of figure 1 shows that magnetic fields amplified in the disk are escaping from the initial disk, although the magnetic field is continuously amplified inside the



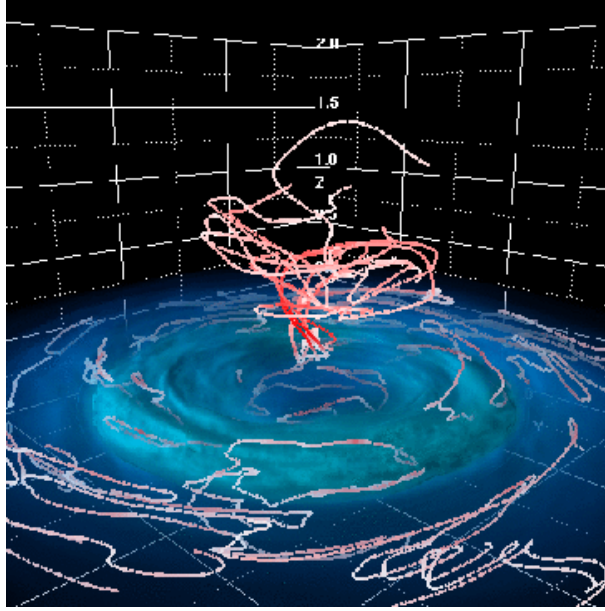


**Fig. 3.** Snapshot of the density distribution (blue color) and magnetic field lines at  $t = 149.5$  ( $\sim 0.7$  Gyr). Blue region shows the volume rendered density and curves show magnetic field lines.

disk by the MRI.

At the initial state of our simulation, magnetic fields do not exist in the inner regions of the disk because we confined the azimuthal magnetic fields only inside the initial gas torus. As MRI grows in the outer disk, the disk gas infalling toward the central region carries in the magnetic fields. The magnetic fields are amplified by MRI within the time scale of several rotation period. The amplification of the magnetic fields saturates when  $\beta \sim 10$ , similarly to the results for accretion disks (e.g.; Machida & Matsumoto 2003). Figure 1 shows that the gas pressure in the galactic central region is higher than that for the outer region. Because of this higher gas pressure and faster rotation, magnetic fields in the inner region grow faster and stronger than those in the outer region. Figure 2d shows the time evolution of the angular momentum transport rate defined by  $\alpha \equiv -\langle B_\omega B_\varphi / 4\pi \rangle / \langle P \rangle$ . Black and gray curves show  $\alpha$  averaged in the same region as figure 2c. The time averaged value of  $\alpha$  is about  $\alpha \sim 0.03$  in the outer region and  $\alpha \sim 0.02$  in the inner region.

### 3.2. Structure of Magnetic Loops in the Coronal Region

Figure 3 shows the density distribution and 3D structure of magnetic field lines. Blue surfaces show the volume rendered image of the density distribution. Bright color indicates the higher density region. Curves in figure 3 show the magnetic field lines. This clearly shows that the magnetic fields become turbulent inside the gaseous disk. Since it is not easy to trace and identify individual magnetic field lines, we need a tool to extract field lines which belong to the same magnetic loop from the numerical results. We identified individual magnetic loops by the



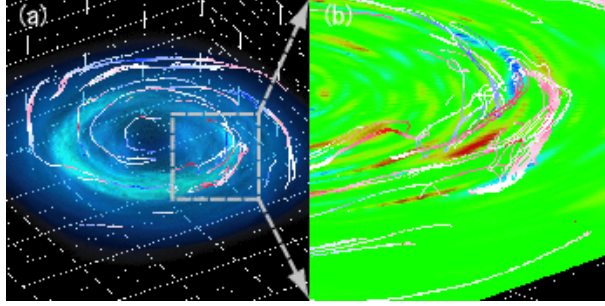


**Fig. 4.** (a) Volume rendered image of density (blue) and magnetic loops (colored curves). Colors on the field lines denote the vertical velocity ( $-0.05 < v_z < 0.05$  blue-white-red). (b) Zoom up image of magnetic field lines inside the gray box in (a). Colored slice shows the strength of the vertical magnetic field. Blue is negative and red is positive.

following algorithm.

1. Choose a horizontal plane  $S(z = z_0)$  which roughly coincides with the disk surface.
2. Magnetic field lines starting from the surface  $S$  are traced by integrating magnetic fields from each grid point on  $S$ . The integration is carried out by 4th-order Runge-Kutta method. Integration step length and maximum number of integration steps are  $\Delta l$  and  $N_s$ , respectively. Integration completes when the integrated field line crosses the original plane  $S$ . The start point  $P_s$  and the end point  $P_f$  reside on the same plane  $S$ .
3. Pick up the magnetic loops which satisfy the following conditions; a) at the starting point, direction of magnetic field is toward the corona ( $B_z > 0$ ), b) it crosses the original plane  $S$  within  $N_s$  steps, c) the distance between the foot-points is longer than  $l_{\min}$ , and d) the length of the magnetic field line  $l$  is longer than 1.
4. Two magnetic field lines are identified as belonging to the same flux tube when the magnetic field lines starting from the point in the neighborhood of  $P_s$  also satisfies all the above conditions and the end point is within  $2\Delta x$  from  $P_f$ . Here  $\Delta x$  is the grid size.

Curves in figure 4 show the examples of magnetic loops identified according to this algorithm. In this analysis, we chose  $\Delta l = \Delta x = 0.02$ ,  $z_0 = 0.1$ , and  $N_s = 200$ . Figure 4 shows the density distribution and the magnetic loops in the region  $-2 < x, y < 2$ , and  $-1 < z < 1$ . Blue surfaces in figure 4a depict the volume rendered image of the density. Magnetic field lines are colored according to the vertical velocity ( $-0.05 < v_z < 0.05$ , from blue to red). We can identify several loop like structures in the coronal region. Figure 4b enlarges the region in dashed-gray box in figure 4a. Colors in the green plane denote the direction of vertical magnetic field. Blue is negative and red is positive. It is clear that approximate height of the loop top is about 0.2 kpc. Small loops continuously rise below the large magnetic loops.

Figure 5 shows the magnetic field lines selected by the same method as those in figure 4. Color denotes the field lines identified as belonging to the same magnetic flux tube. Horizontal slice shows the magnetic energy distribution at  $z = 0.1$ . The inset shows the same flux tubes

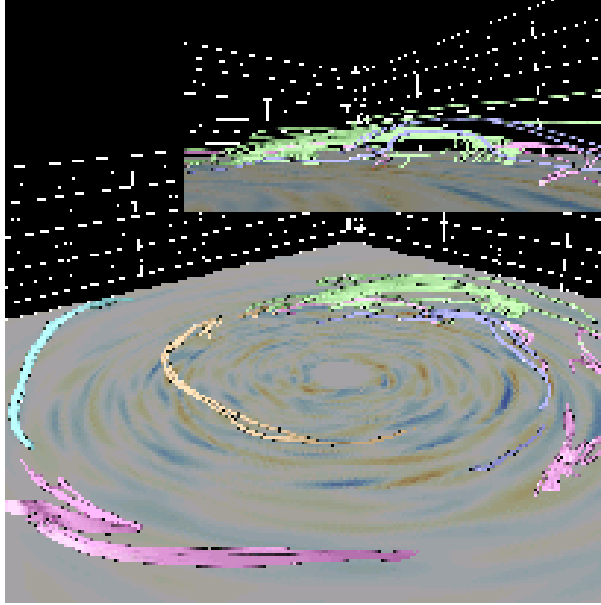


**Fig. 5.** Magnetic field lines in the coronal region. Magnetic field lines depicted by the same color show the magnetic field lines identified as belonging to the same flux tube. Slice locates at  $z = 0.1$ . Color on the slice shows the magnetic energy.

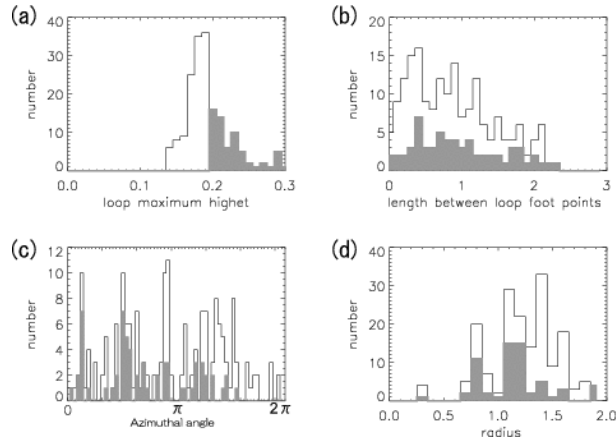


**Fig. 6.** Statistics of magnetic loops. (a) The histogram of the loop maximum height. (b) The histogram of the separation of loop foot points. (c) The azimuthal distribution of the loop top position. (d) The distribution of the radius of the loop tops. Gray shaded ones show the statistics of loops whose maximum height exceeds  $z = 0.2$ .

projected from a different angle. When two or more magnetic field lines are included in the same flux tube (see green curves), we identify them as belonging to the same loop. The loop tops shift toward the outer radius due to the centrifugal force.

Figure 6 shows the statistics of the loops. Although a magnetic flux tube consist of a finite number of magnetic field lines, we chose a representative magnetic field line and let it represent the magnetic flux tube. For example, maximum height of a loop is defined by the

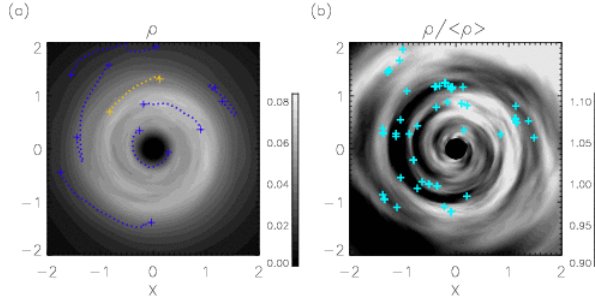


**Fig. 7.** (a) Equatorial density averaged in  $|z| < 0.06$ . Gray scale indicates the density. Dotted curves show the magnetic field lines projected onto the equatorial plane. Symbols denote the position of foot-points of magnetic loops. (b) Equatorial density distribution normalized by the azimuthally averaged density  $\rho/\langle\rho\rangle$ . Crosses denote the position of the loop tops.

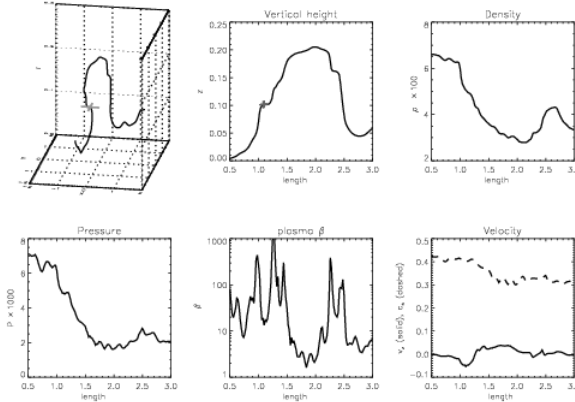
loop top of the representative magnetic field line. We identified 182 magnetic loops in the upper half of the gaseous disk at  $t = 149.5$ . Figure 6a shows the number distribution of the loop top heights. Horizontal axis shows the loop height in unit of kpc. Gray shaded box shows the magnetic loops whose loop top exceed  $z = 0.2$ . Integration of the magnetic field lines start from  $z = 0.1$  plane. We considered only the upper half above the equatorial plane ( $z > 0$ ). Figure 6b shows the histogram of the loop lengths defined by the distance between the loop foot-points. Horizontal axis shows the separation of the foot-points in unit of kpc. Since two distributions in figure 6b are similar each other, the loop height and the loop foot-points distance do not have significant correlations.

Figure 6c shows the azimuthal distribution of the number of magnetic loops. The magnetic loops whose loop top heights exceed  $z = 0.2$  concentrated in  $\pi/2 < \varphi < 3\pi/2$ . However, when we include the loops whose loop top is lower (white boxes), the tendency weakens. The radial distribution of the loop top is shown in figure 6d. Peaks appear around  $\varpi \sim 0.8, 1.1$ , and  $1.4$ .

Next, let us show the distribution of loop tops projected onto the equatorial plane. Figure 7a shows the density distribution around the equatorial plane (averaged in  $|z| < 0.06$ ). Yellow and blue dotted curves show the same magnetic loops displayed in figure 5 projected onto the equatorial plane. Yellow curves correspond to the green loops in figure 5. This figure shows that the density distribution has a  $m = 1$  one-armed distribution near the equatorial plane. Figure 7b shows the normalized density  $\equiv \rho/\langle\rho\rangle$ . Here, we defined the averaged density as follows.

$$\langle\rho\rangle = \int_{-0.06}^{0.06} \int_0^{2\pi} \rho d\varphi dz / \int_{-0.06}^{0.06} \int_0^{2\pi} d\varphi dz . \quad (10)$$

In figure 7b, crosses denote the position of the loop tops. It is shown the magnetic loops are



**Fig. 8.** Distribution of quantities along the loop depicted by yellow curve in figure 7. Right bottom panel shows the vertical velocity (solid) and the sound speed (dashed).

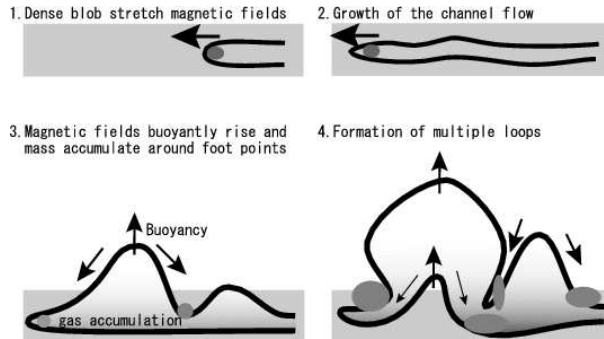
deficient in  $3\pi/2 < \varphi < 2\pi$ . This region corresponds to the higher density region. Loop tops are located near the lower density region, because the magnetic loops often buoyantly rise from the region where magnetic pressure becomes comparable to the gas pressure.

Figure 8 plots the distribution of physical quantities along the magnetic field lines depicted by the yellow curves in figure 7a. Horizontal axis shows the length along the magnetic field lines. Top rows are the 3D view of the magnetic loops, the vertical height, and density from left to right. Bottom rows are the distribution of the gas pressure, the plasma  $\beta$ , vertical velocity and sound speed, respectively. These figures evidently show that magnetic fields are buoyantly rising. That is, the density decreases from the foot points to the loop top. Plasma  $\beta$  inside the loop is about 1. Inside the magnetic loop, the sound speed is almost constant (see figure 8).

## 4. Discussion

### 4.1. Loop Formation and the Origin of Their Concentration

As shown in figures 4 and 5, magnetic loops are formed in the halo region ( $z > 0.1$ ). We identified about 400 loops summing up the upper and lower coronal region. These magnetic loops are concentrated both in certain azimuthal range and radial range (figure 6c, and 6d). Magnetic fields inside the gaseous disk have turbulent component whose amplitude is comparable to the mean azimuthal magnetic fields. Therefore, the magnetic energy shows random patchy structure (see figure 5). On the other hand, one-armed non-axisymmetric pattern develops for density. Magnetic pressure in the low density region becomes stronger than that in the higher density region, because the total pressure is balanced in the disk. Since the magnetic loops with  $\beta \sim 1$  are the most unstable to the Parker instability, buoyantly rising magnetic loops are formed in such lower density region. Thus, non-axisymmetric density distribution



**Fig. 9.** Schematic picture showing the formation of magnetic loops.

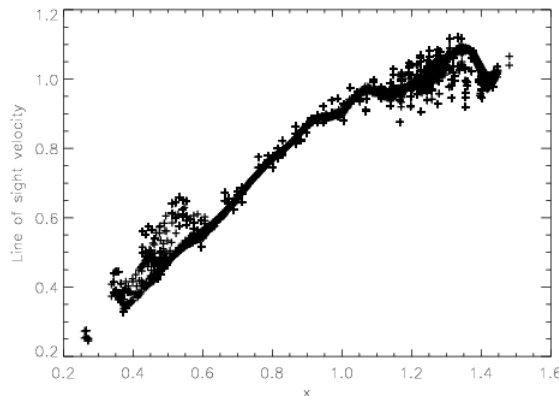


**Fig. 10.** Position-velocity diagram of the mass elements in the loops depicted in green in figure 5. This viewgraph shows the P-V diagram observed from the direction  $\theta = 3\pi/8$ .

results in the azimuthal concentration of magnetic loops.

Figure 9 shows schematically how magnetic loops are formed. As MRI grows, channel flows (e.g., Hawley & Balbus 1992; Sano & Inutsuka 2001; Machida & Matsumoto 2003) create large scale horizontal magnetic fields (figure 9b). When the magnetic energy accumulated in the channel flow becomes comparable to the thermal energy, magnetic loops emerge from the disk by buoyancy (figure 9c, d). This process creates chains of magnetic loops.

#### 4.2. Comparison with Observations

From their millimeter-wave CO observations, Fukui et al. (2006) found two molecular features that look like a loop with a length of several hundred parsecs and width of  $\sim 30$  pc within  $\sim 1$ kpc from the center of our Galaxy. The kinetic energy of these CO loops is about  $\sim 10^{51}$  erg. As shown in figure 5 and 6, our numerical simulation produced magnetic loops whose height  $\sim 200$ pc, width  $\sim 50 - 300$ pc, and length  $\sim 0.1 - 2$ kpc. To compare our simulation with observations, we assumed that the initial gas density is  $\rho_b = 1.6 \times 10^{-24}$ g/cm<sup>3</sup>. In this case the total energy in a loop is about  $10^{51}$  erg.

In CO loops observed in the Galactic center, the line of sight velocity decreases linearly with the length along the loop (see fig.1 in Fukui et al. 2006). Figure 10 shows a position-velocity diagram obtained by our simulation. We plotted magnetic loops colored in green in figure 5. The horizontal axis shows the  $x$ -direction in the Cartesian coordinate system and the vertical axis shows  $y$ -component of the velocity. We assumed that we observed the loops from infinity. Figure 10 shows the linear decrease of the line of sight velocity along the loop. Numerical results indicate that the rotation of the Galactic center gas disk creates this velocity gradient. From figure 10, we can clearly see that foot points show the larger velocity dispersion than the loop top. It can be explained by the large velocity gradient around the foot-points of the magnetic loops where supersonic flow along the magnetic loops collides with the dense disk gas.

Figure 3 shows that a large-scale poloidal magnetic field is created in the innermost region of the Galactic gas disk. Kato, Mineshige & Shibata (2004) showed that magnetic towers are formed by twisting of magnetic loops emerging from a magnetically turbulent accretion disk. Such magnetic towers can be formed even when the initial magnetic field is purely azimuthal (Machida & Matsumoto 2008). The large scale poloidal magnetic fields penetrate the gas disk.

#### 4.3. Mass Supply to the Central 100pc

In our simulations, the unit of mass accretion rate is given by

$$\dot{M}_0 = 33 \left( \frac{\varpi}{1\text{kpc}} \right)^2 \left( \frac{v}{207\text{km/s}} \right) \left( \frac{\rho}{1.66 \times 10^{-24}\text{g/cm}^3} \right) M_\odot/\text{year} . \quad (11)$$

According to figure 2b, mass accretion rate at 200pc in a quasi-steady state is  $\dot{M} \sim 10^{-5}\dot{M}_0 \sim 3.3 \times 10^{-4}M_\odot/\text{yr}$ . This mass accretion rate is determined not by the mass of the central black hole but by the mass of the interstellar gas. Note that the initial density of the 1kpc gas ring we assumed as an initial condition is arbitrary in our simulation. Thus, when dense gas infalls in this region, the accretion rate can be much higher.

The mass accretion rate near the event horizon of the Galactic central black hole SgrA\* is estimated to be less than  $\leq 10^{-8}M_\odot/\text{yr}^{-1}$ , assuming an equipartition magnetic field (e.g., Baganoff et al. 2003). Our simulation indicates the mass accretion rate at  $\varpi = 200$  pc becomes about  $\simeq 10^{-4}M_\odot/\text{yr}^{-1}$ . This may show that the mass accretion rate decreases from  $10^{-4}M_\odot/\text{yr}$  to  $10^{-8}M_\odot/\text{yr}$  in  $0.01\text{pc} < \varpi < 200\text{pc}$  by some mechanism such as star formation, supernova explosions, or by mass outflows.

#### 4.4. Effects of Cooling

In this paper, we ignored the cooling of the gas. Therefore, the gas temperature of the gas disk exceeds  $10^5\text{K}$ . Since this temperature is higher than that of the warm component observed in the Galactic gaseous disk, the disk scale height may be overestimated. Since the most unstable wavelength of the Parker instability is equal to 10 times of the disk scale height,

the loop length in our simulation can be longer than that of the real galaxy. When we consider the radiative cooling, the interstellar gas will decompose into cold phase and the warm phase. Dense molecular clouds will be formed in the foot-points of magnetic loops where interstellar gas accumulates.

In section 4.2, we compared the position-velocity diagram expected from our simulation with the observation. The velocity dispersion at the foot-points is smaller in our simulations than observations. Since the gas temperature and sound speed are overestimated in our simulations, shock waves formed at the loop foot points are weaker than that expected for simulations including cooling. Thus, when we include the cooling, the position-velocity diagram may indicate a large jump similar to that observed in the Galactic center molecular loops.

## 5. Summary

In this paper, we showed that when interstellar gas is supplied to the Galactic central region, magnetic loops are formed due to the buoyant rise of magnetic fields amplified by MRI inside the disk. When the mass of the supplied gas is about  $10^7 M_\odot$ , the magnetic fields can be amplified up to  $10\mu\text{G}$  at 1kpc from the Galactic center. This enables the accretion of the ISM. Mass accretion rate at quasi-steady state is  $\dot{M} \sim 10^{-5} - 10^{-4} M_\odot/\text{yr}$ . Magnetic loops with length 1kpc buoyantly emerge from the disk and form magnetic loops whose maximum height exceeds 200pc. The disk gas slides down along the loop with maximum speed of 30km/s. We developed an algorithm which identify magnetic loops from simulation results. More than 400 loops are identified by applying this algorithm. Typical energy of a magnetic loops is  $10^{51}$  erg. This magnetic energy is consistent with the kinetic energy of the CO loops observed by NANTEN telescope. We found that magnetic loops have preferential azimuthal angle. They tend to rise in regions with higher magnetic pressure (i.e., lower density).

In this calculation, we considered only the warm gas components. However, the Galactic gaseous disk has cooler components. In subsequent papers, we would like to include the gas cooling effects.

We are grateful to Drs. T. Kudoh, K. Wada and K. Asano for useful discussion. Numerical computations were carried out on VPP5000 at Center for Computational Astrophysics, CfCA of NAOJ (P.I. MM). This work is financially supported in part by a Grant-in-Aid for Scientific Research (KAKENHI) from JSPS(P.I. YF:20244014).

## References

- Baek, C. H., Kudoh, T., & Tomisaka, K. 2008, *ApJ*, 682, 434
- Baganoff, F. K. et al. 2003, *ApJ*, 591, 891
- Balbus, S. A., & Hawley, J. F. 1991, *ApJ*, 376, 214
- Beck, R., Brandenburg, A., Moss, D., Shukurov, A., & Sokoloff, D. 1996, *ARA&A*, 34, 155



- Beck, R. 2008, astro-ph 0810.2923
- Brandenburg, A., Nordlund, A., Stein, R. F., & Torkelsson, U. 1995, ApJ, 446, 741
- Chou, W., Tajima, T., Matsumoto, R., & Shibata, K. 1997, PASJ, 49, 389
- Fukui, Y., et al., 2006, Science, 314, 106
- Hawley, J. F., & Balbus, S. A., 2002, ApJ, 400, 595
- Hawley, J. F., Gammie, C. F., & Balbus, S. A. 1995, ApJ, 440, 742
- Kato, Y., Mineshige, S., & Shibata, K. 2004, ApJ, 605, 307
- Hisore, S., Krolik, H. H., & Stone, J. M. 2006, ApJ, 640, 901
- Machida, M., Hayashi, M. R., & Matsumoto, R. 2000, ApJ, 563, 67
- Machida, M., & Matsumoto, R. 2003, ApJ, 585, 429
- Machida, M., Nakamura, K. E., & Matsumoto, R. 2006, PASJ, 58, 193
- Machida, M., & Matsumoto, R. 2008, PASJ, 60, 613
- Matsumoto, R., Horiuchi, T., Shibata, K., & Hanawa, T. 1988, PASJ, 40, 171
- Matsumoto, R., & Tajima, T. 1995, ApJ, 445, 767
- Miyamoto, M., & Nagai, R. 1975, PASJ, 27, 533
- Mizuno, A., & Fukui, Y. 2004, Astronomical Society of the Pacific, Proceedings of ASP Conference, 307, 59
- Morris, M. R., & Serabyn, E. 1996, ARA&A, 34, 645
- Nishikori, H., Machida, M., & Matsumoto, R. 2006, ApJ, 641, 862
- Okada, R., Fukue, J., & Matsumoto, R. 1989, PASJ, 41, 133
- Parker, E. N. 1966, ApJ, 145, 811
- Parker, E. N. 1971, ApJ, 163, 255
- Richtmyer, R. D., & Morton, K. W. 1967, Difference methods for initial-value problems New York: Interscience
- Rubin, E. L., & Burstein, S. Z. 1967, JCoPh, 2, 178
- Sano, T., & Miyama, S., M. 1999, ApJ, 515, 776
- Sano, T., & Inutsuka, S. 2001, ApJ, 561, L179
- Shibata, K., Tajima, T., Steinolfson, R. S., & Matsumoto, R. 1989, ApJ, 345, 584
- Sofue, Y., Fujimoto, M, Wielebinski, R. 1986, ARA&A, 24, 459
- Stone, J. M., Hawley, J. F., Gammie, C. F., & Balbus, S. A. 1996, ApJ, 463, 656